Filament Recycling and Sustained Contractile Flows in an Actomyosin Cortex

William McFadden[1], Patrick McCall[2], Edwin Munro[3,*]

1 Biophysical Sciences Program, University of Chicago, Chicago, IL, USA
2 Department of Physics, University of Chicago, Chicago, IL, USA
3 Department of Molecular Genetics and Cell Biology, University of Chicago, Chicago, IL, USA

*** emunro@uchicago.edu**

Abstract

Fill in abstract later.

Author Summary

In this paper, we develop and analyze a minimal model for 2D active networks based on the cortical cytoskeleton of eukaryotic embryos. Our model introduces a drag-like slip between cross-linked filaments as means to dissipate stored stress, generating a macroscopic effective viscosity. We further introduce an active friction to active stress from microscopic properties. We generate computational simulations based on the model, and demonstrate that active stress is sufficient to drive network contraction only temporarily. By introducing filament recycling, we are able to set up steady state flow profiles such as those found in the cortex of developing embryos and migrating cells. The model is used to calculate phenomenological constants measured in prior experiments. Our analysis sheds insight on potential microscopic control parameters governing broad qualitative differences in 2D active networks. We make our model freely accessible and our methodology transparent to enable other researchers to clearly understand our modeling framework and to build upon our findings.

Introduction

Cortical flow is a fundamental and ubiquitous form of cellular deformation that underlies cell polarization, cell division, cell crawling and multicellular tissue morphogenesis [Bray and White, 1988, Hird and White, 1993]. These flows arise within the actomyosin cortex, a thin layer of cross-linked actin filaments and myosin motors that lies just beneath the plasma membrane [Salbreux et al., 2012]. The active forces that drive cortical flows are thought to be generated by myosin motors pulling against individual actin filaments [Munro et al., 2004]. These forces must be integrated within cross-linked networks to build macroscopic contractile stress. At the same time, cross-linked networks resist deformation and this resistance must be dissipated by network remodeling to allow macroscopic network deformation and flow. How force production and dissipation depend on motor activity, network architecture and remodeling remains poorly understood.

Current models for cortical flow rely on coarse-grained descriptions of actomyosin networks as active fluids, whose motions are driven by gradients of active contractile stress and opposed by an effectively viscous resistance [Mayer et al., 2010]. In these models, gradients of active stress are assumed to reflect spatial variation in motor activity and viscous resistance is assumed to reflect the internal dissipation of elastic resistance due to local remodeling of filaments and/or cross-links [Bois et al., 2011]. A key virtue of these models is that their behavior is governed by a few parameters (active stress and effective viscosity). By coupling an active fluid description to simple kinetic models for network assembly and disassembly and making active stress and effective viscosity depend on e.g network density and turnover rates, it is possible to capture phenomenological descriptions of cortical flow. Models based on this active fluids description can successfully reproduce spatiotemporal dynamics of cortical flow observed during polarization [Mayer et al., 2010], cell division [Turlier et al., 2014, Salbreux et al., 2009], cell motility [Keren et al., 2009, Marchetti et al., 2013] and tissue morphogenesis [Heisenberg and Bellaïche, 2013].

However, to understand how cells exert physiological control over cortical deformation and flow, or to build and tune networks with desired properties *in vitro*, it is essential to connect this coarse-grained description to the microscopic origins of force generation and dissipation within cross-linked actomyosin networks. Both active stress and effective viscosity depend sensitively on microscopic parameters including densities of filaments, motors and cross-links, force-dependent motor/filament interactions, cross-link dynamics and network turnover rates. Thus a key challenge is to understand how tuning these microscopic parameters controls the dynamic interplay between active force generation and passive relaxation to control macroscopic dynamics of cortical flow.

Studies in living cells have documented fluid-like stress relaxation on timescales of 10-100s of seconds [Mayer et al., 2010, Hird and White, 1993, Bray and White, 1988, Hochmuth, 2000, Evans and Yeung, 1989, Bausch et al., 1998]. These modes of stress relaxation are thought to arise both from the transient binding/unbinding of individual cross-links and from the turnover (assembly/disassembly) of actin filaments (ref). Studies of cross-linked and/or bundled actin networks *in vitro* suggest that cross-link unbinding may be sufficient to support viscous relaxation (creep) on very long timescales [Wachsstock et al., 1994, Lieleg et al., 2008, Lieleg et al., 2009, Yao et al., 2011, Liu et al., 2007], but is unlikely to explain the rapid large scale cortical deformation and flow observed in living cells. It has been proposed in the field that rapid actin turnover must play a significant role as well. Indeed, photokinetic and single molecule imaging studies studies reveal rapid turnover of cortical actin filaments in living cells on timescales of 10-100 seconds [Robin et al., 2014]. Previous theoretical models have explored the dependence of stress relaxation on cross-link binding and unbinding analytically [Broedersz et al., 2010, Müller et al., 2014] and others have explicitly modeled reversible cross-linking in combination with complex mechanics of filament bundles [Kim et al., 2011, Lieleg et al., 2009, Lieleg and Bausch, 2007]. However, until very recently [Mak et al., 2016] very little attention has been paid to actin turnover as mechanism of stress relaxation.

Recent work has also begun to reveal insights into mechanisms that govern active stress generation in disordered actomyosin networks. In vitro studies have confirmed that local interactions among actin filaments and myosin motors are sufficient to drive macroscopic contraction of disordered networks [Murrell and Gardel, 2012]. Theoretical studies suggest that asymmetrical compliance of actin filaments (stiffer under extension than compression) and spatial differences (dispersion) in motor activity are sufficient conditions for contraction in one [Lenz et al., 2012] and two [Lenz, 2014] dimensional networks, although other routes to contractility may also exist [Lenz, 2014]. Further work has explored how modulation of network architecture, cross-link dynamics and motor density, activity and assembly state can shape rates and patterns of network deformation [Köhler and Bausch, 2012, Alvarado et al., 2013, Banerjee and Marchetti, 2011] or network rheology [Liverpool et al., 2009, Koenderink et al., 2009].

Significantly, *in vitro* models for disordered actomyosin networks have used stable actin filaments, and these networks support only transient contraction, either because of network collapse [Alvarado et al., 2013], or buildup of elastic resistance (ref? I don't know about this one), or because network rearrangements (polarity sorting) dissipate the potential to generate contractile force [Ndlec et al., 1997, Surrey et al., 2001]. This suggest that continuous turnover of actin filaments may play a key role in allowing sustained deformation and flow. Recent theoretical and modeling studies have begun to explore how this could work [Hiraiwa and Salbreux, 2015, Mak et al., 2016, Zumdieck et al., 2007], and to explore dynamic behaviors that can emerge in contractile material with turnover [Dierkes et al., 2014]. However, there is much to learn about how the buildup and maintenance of contractile force during continuous deformation and flow depends local interplay of network architecture, motor activity and filament turnover.

The goal of this work was to build a computational bridge between the microscopic description of cross-linked actomyosin networks and the coarse grained macroscopic description of an active fluid. We sought to capture the essential microscope features (dynamic cross-links, active motors and semi flexible actin filaments with asymmetric compliance and continuous filament recycling), but in a way that is sufficiently simple to allow systematic exploration of how parameters that govern network deformation and flow in an active fluid theory depend on microscopic parameters. To this end, we introduce several coarse-grained approximations into our representation of filament networks. First, we represent semi-flexible actin filaments as chains of simple springs with asymmetric compliance (stronger in extension than compression). Second, we replace dynamic binding/unbinding of elastic cross-links with a coarse-grained representation in terms of molecular friction [Vanossi et al., 2013, Spruijt et al., 2010, Filippov et al., 2004], such that filaments can slide past each other against a constant fictional resistance. Third, we used a similar scheme to introduce active motors at filament crossover points with a simple linear force/velocity relationship, and we introduce dispersion of motor activity by making only a subset of filament overlaps active [Banerjee et al., 2011]. Finally, we model filament turnover by regularly reseting a subset of filaments to a new unstrained position. Importantly, these simplification allows us to extend our single polymer models to dynamical systems of larger network models for direct comparison between theory and modeling results. This level of coarse graining will therefore make it easier to understand classes of behavior for varying compositions of cross-linked filament networks. In addition, it allows us to compute a new class of numerical simulations efficiently, which gives us concrete predictions for behaviors in widely different networks with measurable dependencies on molecular details.

Models

Our goal was to model essential microscope features of cross-linked actomyosin networks (semi flexible actin filaments with asymmetric compliance, dynamic cross-links, active motors and and continuous filament recycling), in a way that is simple enough to allow systematic exploration of how tuning these microscopic features controls macroscopic network deformation and flow. We focus on 2D networks for computational tractability and because they capture a reasonable approximation of the quasi-2D cortical actomyosin networks that govern flow and deformation in many eukaryotic cells [Mayer

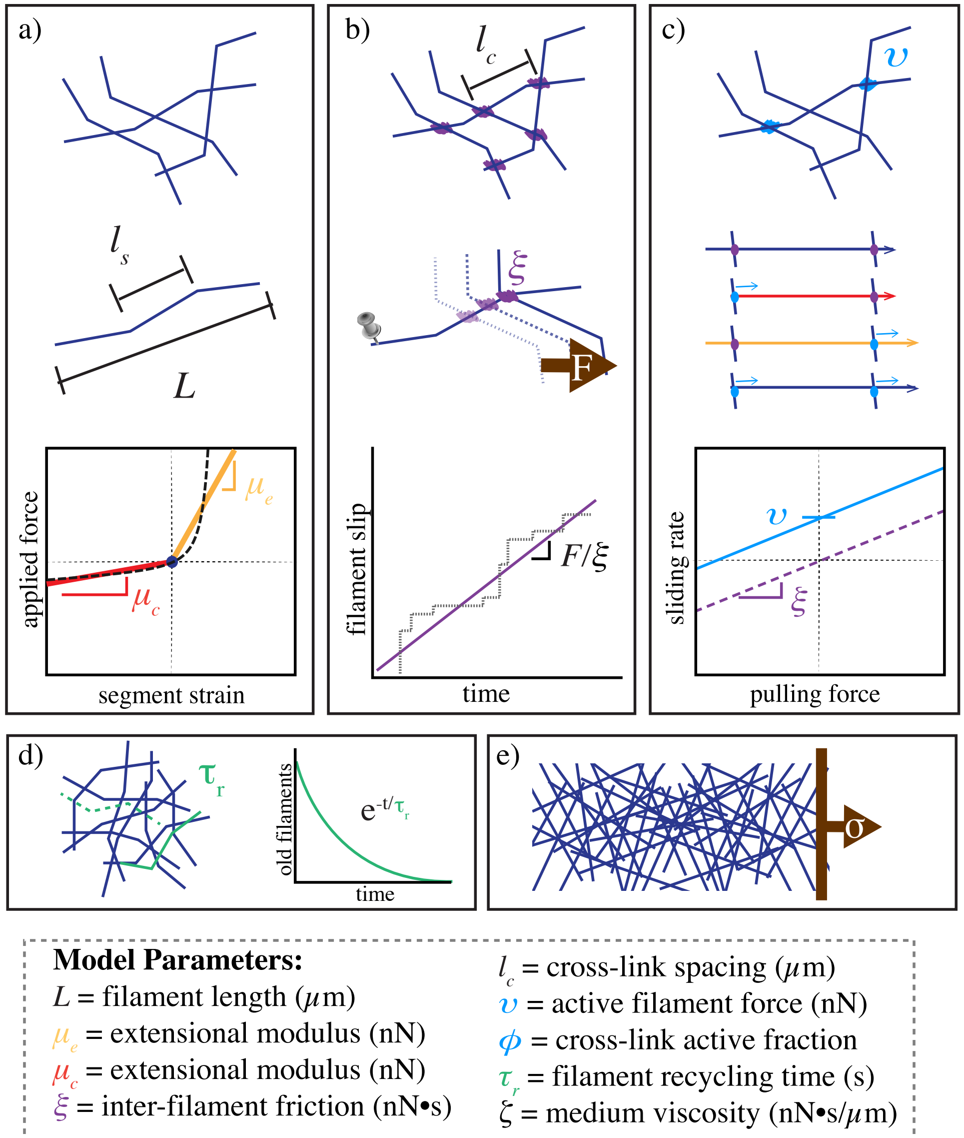

Figure 1. Schematic of modeling framework. a) Asymmetric filament compliance.Filaments have smaller spring constant for compression than for extension. b) Cross-link slip. Cross-links are coupled by an effective drag, such that their relative motion is proportional to any applied force. c) Motor activity. Filament activity manifests as a basal sliding rate even in the absence of an external force. Fractional activity. Only a subset of filament cross-links are active, resulting in differential force exertion along the filament. d) Filament recycling. Filaments are turned over at a constant rate, leading to a refreshing in the strain state of all filaments after a characteristic timescale. e) Applied Stress. In simulations with passive cross-links, and external stress is applied as force filed acting on a fixed spatial domain.

et al., 2010], or the quasi-2D networks used in recent in vitro studies [Murrell and Gardel, 2012, Sanchez et al., 2012].

Asymmetric Filament Compliance

We model individual filaments as chains of springs with relaxed length l_s. Filaments can therefore be represented as a sequence of nodes with positions $\mathbf{x_i}$ and nearest neighbor force interactions, $\mathbf{F_i^\mu}$, of the form

$$|F_i^\mu| = \mu \cdot \frac{|\mathbf{x_{i+1}} - \mathbf{x_i}| - l_s}{l_s} + \mu \cdot \frac{|\mathbf{x_{i-1}} - \mathbf{x_i}| - l_s}{l_s} \tag{1}$$

where the modulus, μ, is a composite quantity representing both filament and cross-linker compliance in a manner similar to a proposed effective medium theory [Broedersz et al., 2009]. To model asymmetric filament compliance, we assign the modulus μ, a different value depending on whether $|\mathbf{x_{i-1}} - \mathbf{x_i}| - l_s$ (the strain) is greater or less than 0. In the limit of highly rigid cross-links and flexible filaments, our model reduces to the pure semi-flexible filament models of [Head et al., 2003, Wilhelm and Frey, 2003]. In the opposite regime of nearly rigid filaments and highly flexible cross links, our method is still largely similar to the model of [Broedersz et al., 2009] in small strain regimes before any nonlinear cross link stiffening. In a departure from those models, we assume here that the magnitude of the force on interior cross-links is the same as those on the exterior. This approach ignores the variation in strain on these two sets of cross-links as addressed in [Broedersz et al., 2009], but we choose to ignore this variation in favor of an approximated, global mean approach.

Drag-like Coupling Between Overlapping Filaments

Previous models represent cross-linkers as elastic connections between pairs of points on neighboring filaments that appear and disappear with either fixed or strain-dependent probabilities [Kim et al., 2011, Broedersz et al., 2009]. Here, we introduce a simpler coarse-grained model for dynamic cross-links by replacing many transient elastic interactions with an effective drag-like coupling between every pair of overlapping segments.

$$\mathbf{F_i^\xi} = \xi \cdot \int_{s_{i-1}}^{s_{i+1}} ds \frac{l_s - |s - s_i|}{l_s} \left(\mathbf{v_i} - \mathbf{v_j}\right) p_{ij}(s) \tag{2}$$

Where $p_{ij}(s)$ represents the locational distribution of cross-link points (equal to 1 at locations of cross-links and 0 elsewhere) and $\mathbf{v_i}$ and $\mathbf{v_j}$ represent the velocities of the ith and jth filament segment. This model assumes a linear relation between applied force and the velocity difference between attached segments. This drag-like coupling has been shown to be an adequate approximation in the case of ionic cross-linking of actin [Ward et al., 2015, Chandran and Mofrad, 2010], and can be found in the theoretical basis of force-velocity curves for myosin bound filaments [Banerjee et al., 2011]. Although non-linearities can arise through force dependent detachment kinetics and/or non-linear force extension of cross-links, we assume that inhomogeneities from non-linear effects are of second or higher order. With this assumption, the motion of filaments can be described by a dynamical equation of the form

$$L\zeta\mathbf{v_i} + \mathbf{F_i^\xi} = \mathbf{F_i^\mu} \tag{3}$$

Here, the first term in the integral is the filament's intrinsic drag through its embedding fluid, ζ, while the second comes from the drag-like coupling between filaments, ξ.

Active Coupling for Motor Driven Filament Interactions

To add motor activity we select a subset of cross-linked points and impart an additional force of magnitude υ directed in the orientations of the individual filaments, $\mathbf{u_i}$. This leads to a modification of the equation of motion to

$$\mathbf{F_i^\upsilon} = \hat{\mathbf{u}}_\mathbf{i} \cdot \upsilon \int ds \sum_j \frac{l_s - |s - s_i|}{l_s} p_{ij} q_{ij} \tag{4}$$

In this formulation, only at the subset of points where $p_{ij} = 1$ and $q_{ij} = 1$ will there be a force imparted. In our simulations we let q_{ij} be selected randomly such that $\bar{q} = \phi$, where $\bar{q}$ indicates the mean of q.

Finally, for each active force, $\mathbf{F_j^\upsilon}$, imparted by filament j, we must also impart the opposite force onto the filament i as well. Therefore, the entire force balance equation with activity will appear as

$$L\zeta \mathbf{v_i} + \mathbf{F_i^\xi} = \mathbf{F_i^\mu} + \mathbf{F_i^\upsilon} - \sum_j \mathbf{F_j^\upsilon} p_{ij} q_{ij} \tag{5}$$

2D Network Formation

We used a mikado model approach [Unterberger and Holzapfel, 2014] to initialize a minimal network of connected unstressed linear filaments in a rectangular 2D domain. We generate 2D networks of these semi-flexible filaments by laying down straight lines of length, L, with random position and orientation. We then assume that overlapping filaments become cross-linked at their points of overlap. Although real cytoskeletal networks may form with non-negligible anisotropy, for simplicity, we focus on isotropically initialized networks. We define the density using the average distance between cross-links along a filament, l_c. A simple geometrical argument can then be used to derive the number of filaments filling a domain as a function of L and l_c [Head et al., 2003]. Here, we use the approximation that the number of filaments needed to tile a rectangular domain of size $W \times H$ is $2WH/Ll_c$, and that the length density is therefore simply, $1/l_c$. In the absence of cross-link slip, we expect the network to form a connected solid with a well defined elastic modulus [Head et al., 2003, Wilhelm and Frey, 2003].

System of Equations for Applied Stress

We model our full network as a coupled system of differential equations satisfying 5. Although the general mechanical response of this system may be very complex, we focus our attention on low frequency deformations and the steady-state creep response of the system to an applied stress. To do this we introduce a fixed stress, σ along one edge of the network. The stress is applied via individual forces to the filaments lying within a patch of size D_w such that the sum of individual forces is equal to the applied stress times the height of the domain. These forces points in the direction, $\hat{\mathbf{x}}$, producing and extension of the patch.

Finally, we add a 0 velocity constraint at the other edge of our domain of interest. We assume that our network is in the "dry," low Reynold's number limit, where inertial effects are so small that we can equate our total force to 0. Therefore, we have a dynamical system of wormlike chain filaments satisfying

$$L\zeta \mathbf{v_i} + \mathbf{F_i^\xi}(\mathbf{v_i}) = \mathbf{F_i^\mu}(\mathbf{x_i}) + \mathbf{F_i^\upsilon}(\mathbf{x_i}) + \sigma \hat{\mathbf{u}}(\mathbf{x_i}) \tag{6}$$

subject to constraints such that $\mathbf{v_i}(\mathbf{x})$ is 0 with $x = 0$. This results in an implicit differential equation for filament segments which can be discretized and integrated in time to produce a solution for the motion of the system.

Filament Recycling as a model for rapid filament turnover

In living cells, actin filament assembly is governed by multiple factors that control nucleation, elongation and filament branching. Likewise filament disassembly is governed by multiple factors that promote filament severing and monomer dissociation at filament ends. Here, we focus on a lowest order model for filament recycling in which entire filaments appear with a fixed probability per unit area per unit time and disappear with a fixed probability per filament per unit time. With this assumption, in the absence of network deformation, the density of filaments will equilibrate to a steady state density with time constant $\tau_r = 1/r_{diss}$. In deforming networks, the density will be set by a competition between strain thinning or thickening, and density equilibration via turnover. To implement this assumption, at fixed time interval $\tau_s < 0.01 \cdot \tau_r$ (i.e. 1% of the equilibration time), we selected a fraction, τ_s/τ_r, of existing filaments (i.e. less than 1% of the total filaments) for degradation. We then generated an equal number of new unstrained filaments to appear within the network at random positions and orientations. This has the effect of creating an approximately exponential decay (with time constant τ_r) in the number of old filaments over time, while maintaining a constant number of total filaments.

Computational Simulation Method

Details of our simulation approach can be found in the Appendix. Briefly, equations 1,2,4 and 6 define a coupled system of ordinary differential equations for the velocities of the endpoints of filament segments, $\mathbf{x}$. These equations are coupled by the effective cross-link friction on segment overlap points, yielding a system of the form:

$$\mathbf{A} \cdot \dot{\mathbf{x}} = \mathbf{f}(\mathbf{x}) \tag{7}$$

where $\mathbf{A}$ represents a coupling matrix between endpoints of filaments that overlap, and $\mathbf{f}(\mathbf{x})$ is the spring force between pairs of filament segment endpoints. We numerically integrated this system of equations to find the time evolution of the positions of all filament endpoints. We generate a network of filaments with random positions and orientations as described above within a domain of size D_x by D_y. For all simulations, we imposed periodic boundaries in the y-dimension. To impose an extensional stress, we constrained all filament segment endpoints within a fixed distance $0.05 \cdot D_x$ from the left edge of the domain to be non-moving, then we imposed a rightwards force on all segment endpoints within a distance $0.05 \cdot D_x$ from the left edge of the patch. To simulation free contraction, we removed all constraints at boundaries; to assess buildup of contractile stress under isometricc conditions, we pinned both left and right edges of the network as described above.

We smoothed all filament interactions, force fields, and constraints over small regions such that the equations contained no sharp discontinuities. The nominal units for length, force, and time are μm, nN, and s, respectively. We explored parameter space around an estimate of biologically relevant parameter values given in Table 1.

Results and Discussion

Our ultimate goal was to characterize how rates and patterns of cortical flow are shaped by complex dependencies of active force generation and passive force dissipation on

Table 1. Simulation Parameter Values

parameter	symbol	physiological estimate
extensional modulus	μ_e	$10nN$
compressional modulus	μ_c	$0.1nN$
cross-link drag coefficient	ξ	$unknown$
medium drag coefficient	ζ	$0.0005\frac{nNs}{\mu m^2}$
filament length	L	$5\mu m$
cross-link spacing	l_c	$0.5\mu m$
domain size	$D_x \times D_y$	$20 \times 50\mu m$

network architecture, local coupling (active and passive) between filaments and filament recycling. We proceeded in three steps: First, we analyzed the passive deformations of cross-linked networks (absent active motors) in response to a constant external force. Next, we analyzed the dynamics of internal stress buildup and dissipation in the same networks, but with active motors, as they contract freely or build force against fixed external boundaries. Finally, we consider the dynamic interplay of internal stress buildup, contraction, and stress relaxation in networks that undergo steady state flow in response to spatial gradients of motor activity.

Filament recycling prevents cortical tearing and modulates the viscous stress relaxation of passive filament networks

Networks with passive cross-links and no filament turnover undergo three stages of deformation in response to an extensional force. To characterize the passive response of a filament network with effective cross-link drag in the absence of filament recycling and motor activity, we imposed an external force on a simulated network, and then quantified the mechanical response in terms of internal network stress and network strain as a function of time. Figure 2a shows the typical response of a simulated network. To quantify this response, we measured the local velocity of the network at different positions along the axis of deformation as the mean velocity of all filament segments intersecting that position; we measured the internal network stress at each position by summing the axial component of the tensions on all filament segments intersecting that position, and dividing by network height; finally, we measured network strain rate as the average change in filament position divided by its original position.

During early (not shown) and intermediate (Figure 2b) stages of the deformation, the internal stress (blue) was nearly constant throughout the material while the velocity (orange) increased linearly with distance from the site network attachment, indicating approximately constant deformation (strain) rate throughout the material. Accordingly, we characterized the network response in terms of time-dependent bulk material stress and strain rates.

Plotting the material stress and strain averages as a function of time revealed that the deformation occurred in three qualitatively distinct phases (Figure 2a,c). On short timescales the network exhibited a viscoelastic response, characterized by a rapid buildup of internal stress and a rapid exponential approach to a fixed strain, representing the elastic limit in the absence of cross-link slip predicted by [Head et al., 2003]. On intermediate timescales, the internal stress remained constant while the network continued to deform slowly and continuously with nearly constant strain rate (shown as dashed line in Fig 2c) as filaments slipped past one another against the effective cross-link drag. This linear relationship between strain and time characterizes a material with an effective viscosity, η_c, given by the ratio of the applied stress to the strain rate. We define the transition time between this fast, viscoelastic response and the slower, effectively viscous deformation phase as (τ_c). Finally, as the network strain approached a critical value ($\sim 30\%$ for the simulation in Figure 2), strain thinning led to decreased network connectivity, local tearing, and acceleration of the network deformation (see inset in Figure 2c). This eventually resulted in the highly heterogeneous network structure shown in the t=440sz example of Figure 2a.

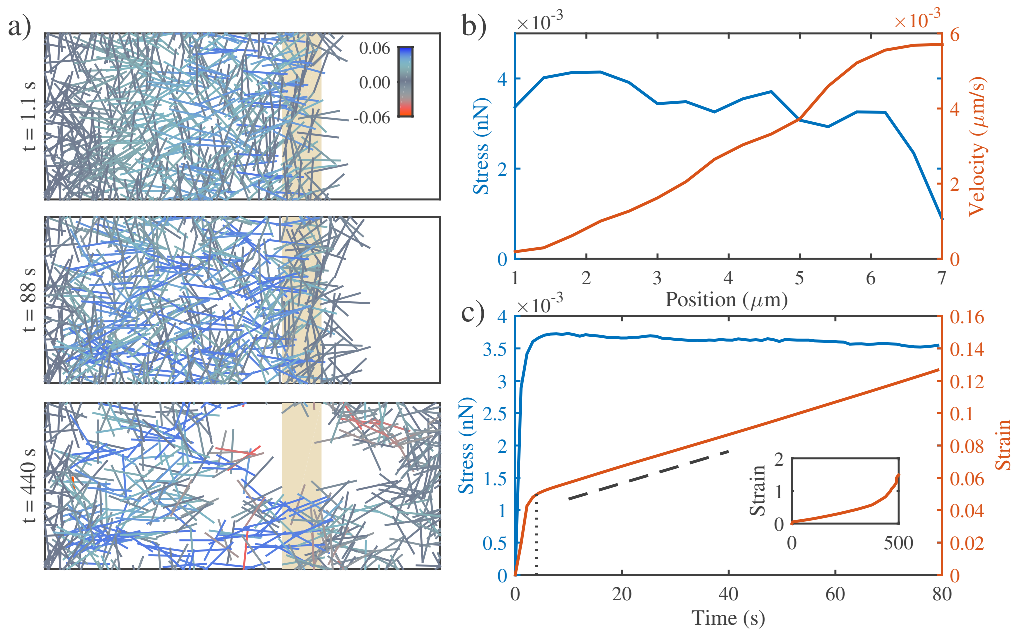

Figure 2. Networks with passive cross-links and no filament turnover undergo three stages of deformation in response to an extensional force. **a)** Three successive time points from a simulation of a $4 \times 10\,\mu m$ network deforming under an applied extensional stress of 0.005 $nN/\mu m$. In this and all subsequent figures, filaments are color-coded with respect state of stress (blue = tension, red = compression). Network parameters: $L = 1\,\mu m$, $l_c = 0.3\,\mu m$, $\xi = 100\,nN \cdot s$. **b)** Mean filament stress and velocity profiles for the network in (a) at t=88s. Note that the stress is nearly constant and the velocity is nearly linear as predicted for a viscous fluid under extension. **c)** Plots of the mean stress and strain vs time for the simulation in (a), illustrating the three stages of deformation: (i) A fast initial phase accompanies rapid buildup of internal network stress; (ii) after a characteristic time τ_c s (indicated by vertical dotted line) the network deforms like a material with a constant effective viscosity, η_c, as indicated by the slope of the dashed line. (inset) At long times, the strain accelerates as the network undergoes strain thinning and eventually tears.

Network architecture sets the rate and timescales of deformation. To better understand how network architecture and cross-link dynamics control effective viscosity and the timescale for transition to viscous behavior, we systematically varied network parameters and measured the elastic modulus, G_0, effective viscosity, η_c, and transition time, τ_c, in response to a fixed external stress. For the entire range of network parameters that we sampled, we observed a transition from a fast viscoelastic response to slow effectively viscous deformation. A previous model [Head et al., 2003] for a network of semi-flexible filaments with irreversible cross-linking predicted a closed form solution for the elastic modulus, $G_0 \sim \mu/l_c$, which agrees closely with the elastic limit that we observe during the initial viscoelastic phase (S2 Fig). During the second, effectively viscous phase, filaments slide continuously past one another against the frictional cross-link resistance. A simple theoretical analysis (shown in S1 Text) predicts that the effective viscosity in this regime should be proportional to the effective cross-link drag coefficient of the individual cross-links and to the square of the number of cross-links per filament, with a constant of proportionality $\pi/4$. As shown in Figure 3a, our simulations agree well with this prediction for a large range of network parameters. For many linear viscoelastic materials, the ratio of the elastic modulus, G_0, to the viscosity η_c, is a general indicator of the transition timescale from elastic to viscous behavior [McCrum et al., 1997]. Using our approximations of the elastic modulus and viscosity, we predict a crossover time, $\tau_c \approx L^2\xi/l_c\mu$. By measuring the time at which the strain rate became nearly constant we obtained an estimate of this time for a wide variety of simulation parameters. As shown in Figure 3b, our approximation is in good agreement with the observed transition time, indicating that our simulations are well represented by effectively linear bulk properties.

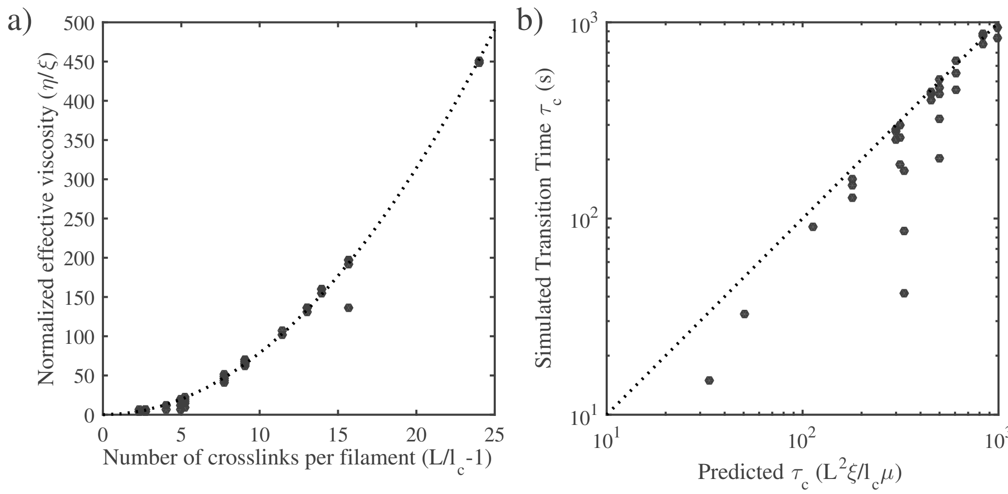

Figure 3. Network architecture sets the rate and timescales of deformation. **a)** The effective viscosity depends on the drag coefficient and the density of the network. Data points are the normalized effective viscosity from simulations (effective viscosity measured in fluid phase divided by the cross link friction coefficient) vs the number of cross links per filament $(L/l_c - 1)$. Dotted line indicates the relationship predicted by a simple theory, $\eta_c = \xi(L/l_c - 1)^2$ **b)** The transition to viscous behavior occurs at a characteristic time, τ_c, that is set by the ratio of the elastic modulus predicted in [Head et al., 2003] (i.e. $G_0 \approx \mu/l_c$) to the effective viscosity, η_c.

Filament recycling rescues network tearing and modulates effective viscosity. To explore how the passive network response to an applied force changed in the presence of filament recycling, we ran a series of simulations with identical filament lengths and network densities and cross-link drag coefficients, while varying the rate of filament recycling. Figure 4a illustrates the results for a particular set of network parameters. In the absence of filament recycling, strain thinning and network tearing lead to a rapid increase in strain rate above a critical strain of $\sim 40\%$.

In contrast, decreasing the filament recycling time led to a progressive increase in the rate of network deformation during the effectively viscous phase and an increase in the critical strain at which the network began to tear. Below a critical recycling time (τ_{crit}), the network could sustain effectively viscous deformation, as shown by the lack

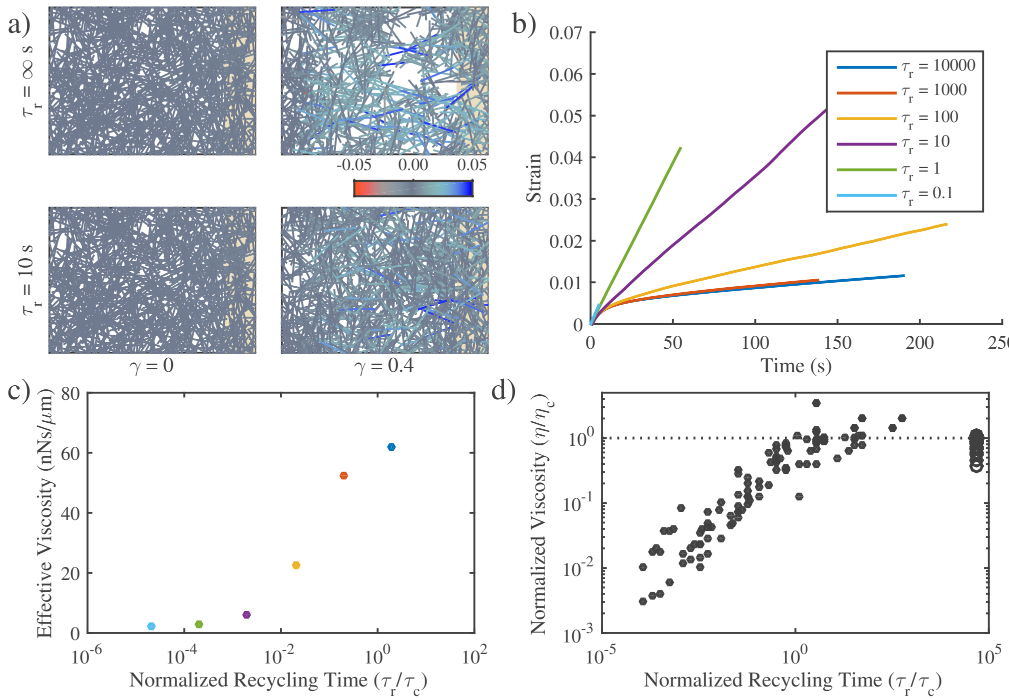

Figure 4. Filament recycling modulates effective viscosity in two regimes. **a)** Examples of $20 \times 12\mu m$ network under 0.001 $nN/\mu m$ extensional stress with recycling ($\tau_r = 10s$) and without, ($\tau_r = \infty$). Both images are taken when the patches had reached a net strain of 0.4. The network with recycling doesn't appear to change shape because its components have been recycled to remain in the original domain. Network parameters: $L = 3\,\mu m$, $l_c = 0.5\,\mu m$, $\xi = 10\,nN \cdot s$. **b)** Strains curves for identical networks with varying levels of filament recycling. Network parameters: $L = 3\,\mu m$, $l_c = 0.5\,\mu m$, $\xi = 10\,nN \cdot s$. **c)** Plotting the effective viscosity derived from the slopes of the lines in panel a. The values have been normalized to the predicted effective viscosity. **d)** Normalized effective viscosities as a function of the normalized recycling time. When the recycling timescale is significantly less than the passive relaxation timescale, the viscosity of the network becomes dependent on recycling time.

of strain thinning in the strain profiles of Figure4b. This steady state deformation is achieved when the rate of filament depletion by strain thinning is stably balanced by a high enough rate of filament reassembly.

The prevention of tearing is directly due to the replenishment of strain thinning in the patch by filaments being recycled back into the domain of applied force. Therefore, we can find the level of filament recycling required to maintain an indefinite viscous flow by analyzing the balance of density lost to straining vs the filament replenished by recycling. The equation for the change in filament length density, ρ, depends both on filament recycling ($k_{app} - k_{diss}\rho$)and strain thinning ($-\dot{\gamma}\rho$). These terms can be rewritten to give the following

$$\frac{d\rho}{dt} = \frac{\rho_0 - \rho}{\tau_r} - \frac{\sigma}{\xi\eta_c(\rho)}\rho \tag{8}$$

where $1/\tau_r$ has been substituted for k_diss, and $\rho_0 = k_{app}\tau_r$. For our networks, the effective viscosity, η_c, is dependent on the filament density (through l_c) so this dependence must be included. Solving this equation for its steady states, and replacing the initial density, ρ_0, with the length density approximation, $1/l_c$, we find that a steady state density only exists under the condition $\tau_{crit} = \eta_c/4\sigma$.

Reducing recycling time, τ_r, below τ_{crit} produced different effects on steady state deformation rates depending on the relative values of τ_r and τ_c, the characteristic time for transition to effectively viscous deformation in the absence of recycling. For $\tau_r > \tau_c$, the effective viscosity remained $\sim$constant with decreasing τ_r; for $\tau_r < \tau_c$, effective viscosity decreased linearly with decreasing τ_r. The intuitive explanation for this is as follows: For $\tau_r > \tau_c$, the deformation rate is dominated by cross-link resistance to sliding of strained filaments. For $\tau_r < \tau_c$, the deformation rate is limited by the level of elastic stress on partially strained filaments; By replacing partially strained with unstrained filaments, the network is able to tune the mean level of stress and thus the deformation rate.

Plotting effective viscosity as a function of decreasing recycling times for this choice of network parameters revealed sharp decrease in effective viscosity as the recycling time exceeded τ_c.

An intuitive explanation for this effect is that rapid recycling increases the network's ability to sustain the faster deformation rate that occurs during the initial viscoelastic response to applied stress. By constantly turning over strained network elements and replacing them with unstrained filaments, the network is able to dissipate stored elastic stress and remain in the viscoelastic response regime indefinitely.

To confirm this relationship more generally, we measured the network deformation rates while varying filament recycling times (Figure 4b). Indeed, by plotting plotted the normalized effective viscosity (ratio of effective viscosity with recycling to effective viscosity without recycling, η_c) vs a normalized recycling rate (recycling time scaled by τ_c), we found that the normalized effective viscosity measured during steady state flow begins to decrease when the recycling time falls below τ_c and below this value the effective viscosity falls off linearly with recycling time to minimal values (Figure 4c).

To describe this we introduce (based on linear viscoelastic models of [McCrum et al., 1997]) an effective recycling viscosity, η_r, which can be tuned between the τ_r dependent and independent regimes, depending on the value of the recycling timescale.

$$\frac{1}{\eta_r} = \frac{1}{\eta_c} + \frac{1}{G_0\tau_c} e^{-\tau_r/\tau_c} \tag{9}$$

In long $\tau_r \gg \tau_c$ limit, this simplifies to $\eta_r = \eta_c$, while in the short $\tau_r \ll \tau_c$ limit, this simplifies to $\eta_r \sim \tau_r$, which matches qualitatively with our estimate as found in Figure 4d for a large range of parameters. This model presents a simple quantitative description of our simulation data.

In summary, our results suggests that filament recycling plays several key roles in controlling passive deformations of cross-linked networks in response to extensional stress. Tuning recycling rates above a critical value allows networks to undergo continuous viscous deformation, for long times, without tearing, for a wide range of different effective viscosities and deformation rates. Above this critical value, modulating filament recycling rates can tune the network to operate in either of two regimes. At intermediate recycling timescales, the deformation is limited by effective cross-link friction, the effective viscosity depends on the strength of inter-filament cross-linking and the network's architecture, and is relatively insensitive to changes in recycling rate. For recycling times below τ_c, the deformation is governed by the buildup of elastic stress on network filaments, and effective viscosity becomes strongly dependent on recycling time.

These findings are in agreement with previous simulations on effective viscosity in cross-linked networks. A previous analysis [Kim et al., 2014] looked at the effect of a different form of filament turnover in networks with irreversible cross-linking. The authors also showed two regimes of deformation: one in which network deformation was linearly viscous and tuned by the turnover rate, and one where the creep rate was set purely by the turnover rate independent of applied force. Although the implementation is different, the two regimes observed in our model are in qualitative agreement and arise from similar microscopic origins. Specifically, the short recycling time regime, where the mechanics are governed by filament extension, is directly equivalent in both models. For this regime, our model is able to give a theoretical description of the effective viscosity found in [Kim et al., 2014]. For the opposite regime of long recycling times, the models have a distinct difference. For the model of [Kim et al., 2014] there was no cross-link unbinding so without of filament turnover, the network would not deform beyond its elastic limit. In contrast, our simulations always require non-zero cross-link slip so there is always some viscous network deformation. Therefore, in the regime of long recycling times our model approaches the limit of cross-link dominated viscosity whereas the model of [Kim et al., 2014] approached an infinite viscosity limit.

Filament recycling allows persistent stress buildup in active networks

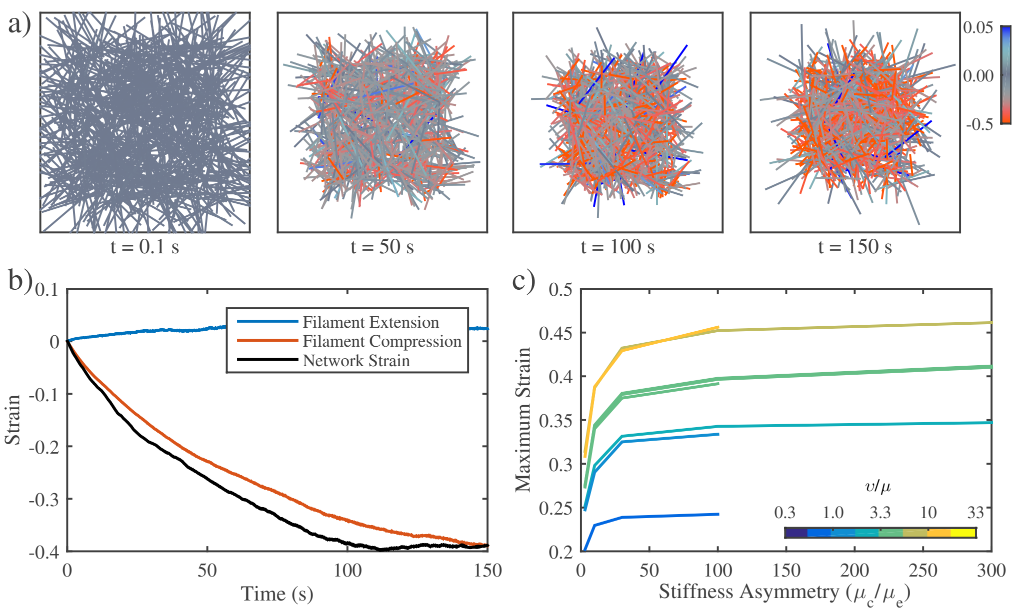

Figure 5. In the absence of filament recycling, active networks with free boundaries contract and then stall against passive resistance to network compression. **a)** Example of an active network contracting. Note the buildup of compressive stress as contraction approaches stall between 100 s and 150 s. Network parameters: $L = 5\,\mu m$, $l_c = 0.3\,\mu m$, $\xi = 100\,nN \cdot s$, $\upsilon = 0.1\,nN$. **b)** Plots showing time evolution of total network strain and the average extensional (blue) or compressive (red) strain on individual filaments. **c)** The network's ability to deform requires asymmetric filament compliance. Total network strain also increases with the applied myosin force υ.

In the absence of filament recycling, active networks with free boundaries contract and then stall against passive resistance to network compression. We next introduced active motors into our network model. Previous theoretical and experimental studies [Lenz et al., 2012, Murrell and Gardel, 2012, Koenderink et al., 2009] suggested that a minimal condition for contraction of disordered networks is dispersion in motor force. In our model, we introduced this dispersion by placing active motors at a fraction of filament overlap points, such that motors induce compressive or extensional stress along segments of filaments depending on filament orientation and motor occupancy at segment endpoints (Figure 1c).

To test if our minimal implementation of these two requirements (see above) was sufficient to produce macroscopic contraction, we simulated active networks that were unconstrained by external attachments. Indeed, when we turn on motor activity in an initially unstrained network at $t = 0$, we observed a rapid initial contraction, followed by an ∼exponential approach to stall. On a longer timescale, polarity sorting of individual filaments, as previously described [Ndlec et al., 1997, Surrey et al., 2001] rearranged the entire network, undoing the initial contraction (see S2 Video)

We found that our simulation axioms were able to produce transient contraction of a patch of free-floating network. When an initially unstrained network has internal motor activity "switched on" at $t = 0$, the area of the patch begins to decrease with three phases of deformation: rapid initial contraction, stall against compressive resistance, and, finally, filament sorting. These three phases are highly related to the three phases found in the deformation of passive networks described above. As shown in Figure 5a, by 100 s, the network has contracted by 40%, and many internal filaments can be seen to have reached a compressed state (indicated by orange). By 150 s, the compression has stalled, and filament sliding has begun to sort some filaments away from the center. Over long time periods, this filament sorting (previously described in [Ndlec et al., 1997, Surrey et al., 2001]) actually rearranges the entire network, undoing the initial contraction (see S2 Video); however, this sorting phase was not the focus of our current work.

By monitoring both the network and individual filament strains, as in Figure 5b, we found that the initial rapid phase of network deformation is accompanied by rapid compression of individual filaments, as observed experimentally by [Murrell and Gardel, 2012]. Due to the strong stiffness asymmetry, there is far more compressive strain than there is extension in the network. It is this asymmetry that generates the net contraction in a disordered network despite myosin activity being equally capable of generating both. The network contraction stalled over the same timescale as individual filaments, further indicating the essential role of filament compression in generating contractility.

The final contraction extent was strongly dependent on the magnitudes of both the filament stiffness asymmetry (i.e. the ratio of the extensional and compressive stiffnesses μ_e/μ_c) and the motor activity strength (υ). As shown in Figure 5c, small stiffness asymmetries lead to less overall contraction, while larger asymmetries appear to approach some asymptotic limit once they reach a ratio of ~ 100. Additionally, contraction would only occur when there was fractional motor activity, $0 < \phi < 1$, (see S3 Fig). Finally, we found that the contraction consistently stalled over a time scale, $\tau_m =$ (see S3 Fig), indicating that the network architecture also plays a role in setting the timescale of contraction. These findings of the minimal requirements for contractility are all in direct accordance with the theoretical predictions of [Lenz et al., 2012] and [Lenz, 2014]. In fact, we find that removing any single factor from this simulation framework leads to a loss of contraction, suggesting that this system may represent a minimal model of contractility.

Active networks can only exert a transient force against a fixed boundary in the absence of filament recycling. In networks undergoing active motor-driven cortical flow, the rates of contraction in regions of high motor activity, (thus the time to stall), will be limited by the passive resistance of neighboring regions with low motor activity. Therefore, we considered the scenario in which an active network contracts

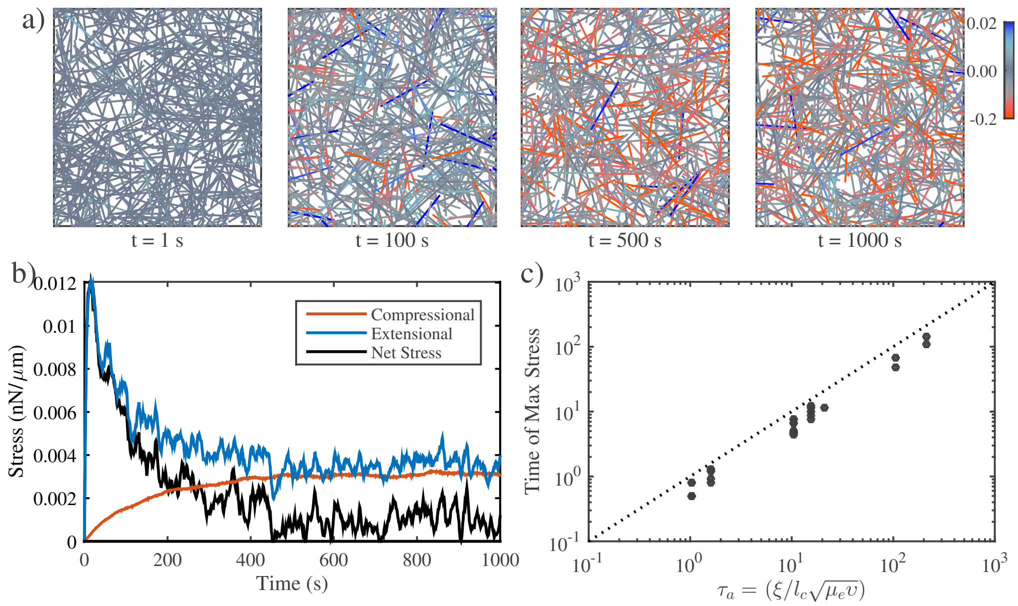

Figure 6. In the absence of filament recycling, active networks can only exert a transient force against a fixed boundary. **a)** Simulation of an active network with fixed boundaries illustrating progressive buildup of internal stress through local filament rearrangement and deformation. Note the progressive buildup of compressive stress on individual filaments. Network parameters: $L = 5\,\mu m$, $l_c = 0.3\,\mu m$, $\xi = 100\,nN \cdot s$, $\upsilon = 0.1\,nN$. **b)** Plots of total network stress and the average extensional (blue) and compressive (red) stress on individual filaments for the simulation shown in (a). Rapid buildup of extensional stress allows the network transiently to exert force on its boundary, but this force is dissipated at longer times as as internal extensional and compressive stresses become balanced. **c**. Measurement and prediction of the characteristic time (τ_a) at which the maximum stress is achieved.

against a fixed resistance by analyzing the stress buildup in a patch that was constrained to maintain its original area. The results from Figure 6a echo those from Figure 5a, with a consistent buildup of internal filament strain (represented by the colored lines) that stabilizes and persists indefinitely. In contrast, the network in Figure 6a does not demonstrate any apparent large-scale rearrangement as any net deformation is impossible since the patch sits in a domain with periodic boundaries.

Under these conditions, we found that a net stress was generated throughout the material, but similar to the results for contraction in Figure 5, the net stress could not be maintained. As shown in Figure 6b, the net stress (black line) initially increases to a maximum σ_a, but then decays back to 0 over longer times. However, the internal compressive and extensional stresses do not decay away entirely. Instead, after the peak stress is reached, the internal stresses become balanced leading to an apparent net stress of approximately 0 despite a nonzero internal stress.

Finally, we measured the time of peak stress and found it consistently occurred with a characteristic time, $\tau_a = \xi/l_c\sqrt{\mu\upsilon}$, as shown in Figure 6c.

Filament recycling allows networks to exert sustained stress on a fixed boundary. We next added filament recycling to simulations with activity, and found that the presence of recycling (1) prevents catastrophic tearing and (2) modulates the level of steady state stress. Similar to the mechanism for preserving integrity in passive

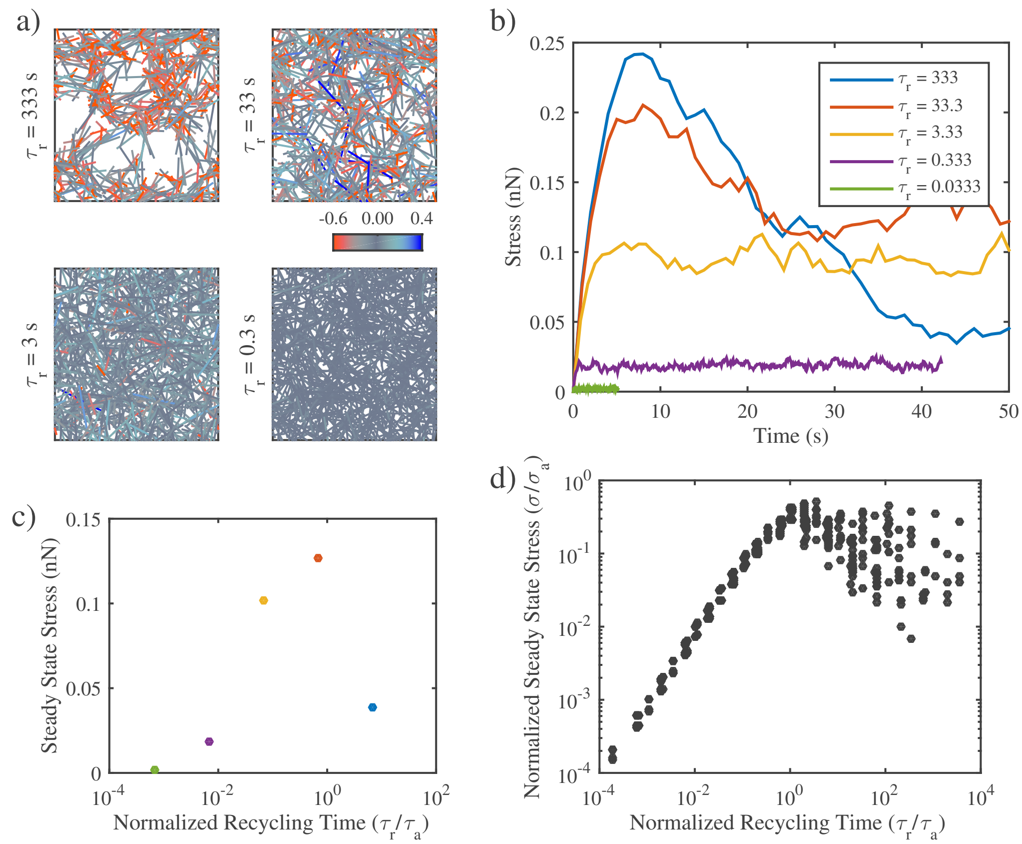

Figure 7. Filament recycling allows network to exert sustained stress on a fixed boundary. **a)** Example simulations of active networks and fixed boundaries for different timescales of filament recycling. Network parameters are the same as in Figure 6, except that the active force (v = 1) has been increased to emphasize the effects of internal network remodeling under stress. Note that significant remodeling occurs for longer recycling times. **b)** Plots of net stress for different recycling times; for long-lived filaments, stress is built rapidly, but then dissipates. Increasing filament turnover rates reduces stress dissipation by recycling compressed filaments; however, very short recycling times prevent any stress from being built up in the first place. **c)** Plotting the steady state stress derived from the slopes of the lines in panel b. The values have been normalized to the predicted effective viscosity. **d)** Normalized steady state stress as a function of normalized recycling time. The steady state stress is set by the timescale at which the network strain is refreshed relative to the timescale at which the max stress is reached.

networks, the recycling appears to refresh the network such that subsets of filaments are continually transitioning from an unstressed to their stressed state before being recycled back to the unstressed state. The presence of recycling therefore both repaired structural inhomogeneities and reset the net strain of individual filaments. The panels in 7a show the differences in structure for identical starting architectures in the presence of different recycling timescales.

Upon the addition of filament recycling, we found that the network maintained a nonzero net stress for timescales much longer than τ_a. We refer to this as the steady state stress because, based on our simulations, it doesn't appear that this stress ever subsides. As can be seen in Figure 7b, The profile of stress buildup changes dramatically by changing the recycling timescale in identical networks corresponding to those in Figure 7a. The effect of changing recycling time is bimodal: As the recycling time is decreased from 333 to 33.3, we can see that the long-term steady state increases from nearly 0.05 to 0.15. Nevertheless, the final steady state is still lower than the peak stress for those curves. In contrast, for the faster recycling rates (3.33, 0.33, 0.033), the final steady state decreases monotonically with decreasing recycling time. In addition, for these shorter timescales, the stress never reaches a peak but rather rises immediately to its steady state level. We attribute this to the strain resetting whereby individual filaments repeatedly are set to an unstrained state and then transition to having more strain until they are again reset. The transition timescale between the increasing and decreasing steady state stress regimes is set by the peak stress time, τ_a, in the absence of recycling as described above.

Filament recycling tunes the balance between active stress buildup and viscous stress relaxation to generate flows

We have shown that filament recycling has a strong impact on both passive and active properties of networks. We ultimately wish to show how filament recycling impacts flows. Active fluid theories propose that flow can be explained in terms of the interplay between active stress and effective viscosity. Therefore, we next tested whether we could measure the effect of recycling on flow in networks with both an active and a passive domain.

Filament recycling tunes the magnitudes of both effective viscosity and steady state stress. To begin, we repeated the single domain (passive or active) simulations while varying all of our networks microscopic parameters. By exploring the effect of these parameters on the output variables we were able to determine the general form of the dependence. In Figure 4d, we illustrate the data collapse of all our simulation results (see S1 Table for details of parameter exploration). Interestingly, both the viscosity (in Figure 4d) and stress (in Figure 7d) show changes in behaviors on either side of their respective governing timescales (τ_c for viscosity and τ_a for active stress). Effective viscosity was found to be independent of recycling time until recycling time became of the same order as the elastic to viscous crossover timescale, at which point it decreased with decreasing recycling time. Similarly, the steady state stress increases with increasing recycling time until it reaches the point of peak stress buildup. From that point it decreases with increasing recycling time.

Filament recycling allows sustained flows in networks with non-isotropic activity. To clearly interrogate the mutual dependencies of effective viscosity and active stress, we next combined passive and active elements in the same simulations. As illustrated in Figure 8a, we generated networks where the left side of the domain contained only passive cross-linkers, while the right side contained a mix of active and passive cross-links. In these networks, we observed a sharp dependence of flow behavior on filament recycling rate. In the $\tau_r = 1000s$ case, filaments deformed more extensively (orange lines), and the network developed noticeable spatial heterogeneity. On the other hand for shorter recycling time of $\tau_r = 33$ s, the network remained much more connected and filaments underwent less total compressional strain. We measured the flow profile across the entire simulation and observed that in both cases the flow field converged on the region at the midline (see S6 Fig) in a manner highly similar to physiological flow profiles found in e.g. *C. elegans* embryos. However, there were large differences in the magnitude and duration of the resulting flows which depended on the recycling time.

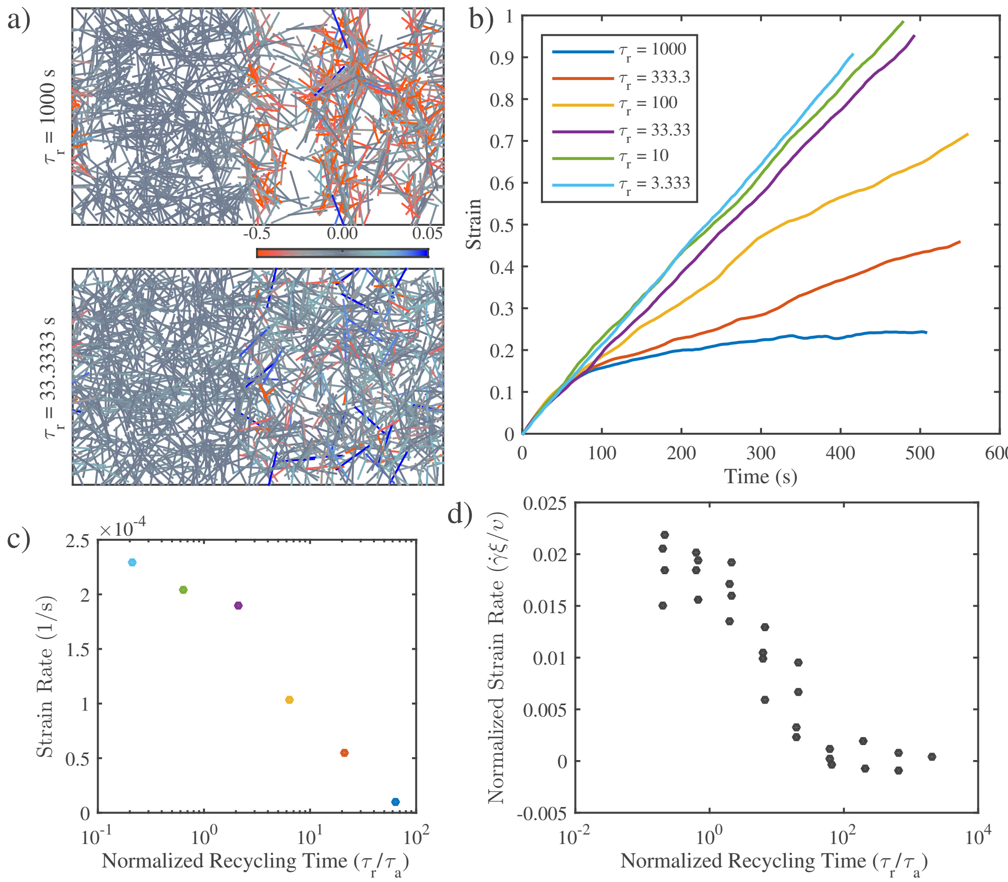

Figure 8. Filament recycling allows sustained flows in networks with non-isotropic activity. **a)** Example simulations of non-isotropic networks with long ($\tau_r = 1000$) and short ($\tau_r = 33$) recycling timescales. In these networks the left half of the network is passive while the right half is active. Network parameters are same as in Figures 6 and 7. **b)** Graph of strain for identical networks varying recycling timescales. With long recycling times, the network stalls; reducing the recycling timescale allows the network to persist in its deformation. However, for the shortest recycling timescales, the steady state strain appears to approach an asymptotic limit. **c)** Graph of network long-term strain rate as a function of recycling timescale for simulations in a) and b). **d)** Graph of network long-term strain rate as a function of recycling timescale across a wide range of parameter space. Note that networks only begin to maintain long-term flows when the recycling time is less than $100\tau_a$.

To understand the time progression of the flow profile, we measured the average network strain over time. From this measurement, we could see a sharp dependence of the behavior on the recycling time, as shown in Figure **??**b. For very long recycling times ($\tau_r = 1000$, dark blue line), the network showed a rapid initial deformation that quickly reached its limit and stalled. However, with decreasing filament recycling times, we found the network was able to sustain its deformation and that the long term strain rate rose toward an asymptotic limit. At the shortest recycling timescales measured, we still saw the effective viscosity remaining relatively high, indicating that for sufficiently short recycling times the effective viscosity may approach an asymptotic flow rate.

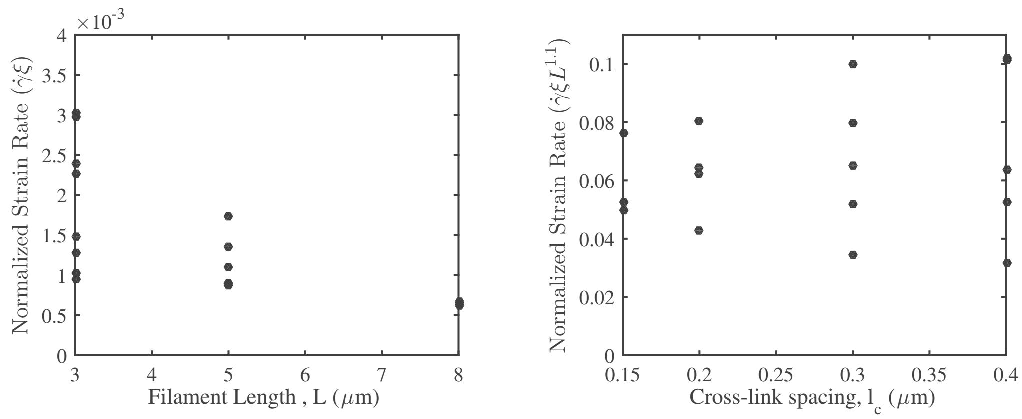

Figure 9. Filament recycling enables macroscopic flows and introduces filament length control over flow rate. **a)** For a fixed filament recoiling time, filament length tuned network deformation rate. **b)** Recycling rate is independent of cross-link spacing in this parameter space.

Filament recycling tunes macroscopic flows and sets architectural control over flow rate. As a final point, we wished to mention what happens when filament recycling is held constant and other parameters are changed. Interestingly, we found surprising architectural dependence for network architectures very closely poised to our physiological estimates. In that regime, filament length was able to tune networks between a low flow and a high flow mode with close to $1/L$ dependence. We believe this may be due to the difference in L dependence between the timescales of effective viscosity and stress buildup.

Conclusion

Our work aimed to create a simulation framework that would allow us to analyze the origins of macroscopic flow in terms of a handful of physiologically relevant microscopic parameters. Toward this aim we developed a minimalist model of a 2D filament network and analyzed the network's reaction to a variety of situations. We found mathematical relationships that determined both the passive effective viscosity and the active stress generation of networks with and without recycling. From these relationships we were able to make predictions about the .

Importantly, our work brings a theoretical understanding to the importance of actomyosin turnover in producing and maintaining long-term large scale flows. This is not entirely surprising due to the abundance of physiological mechanisms for generating network turnover. We propose the concept of "filament recycling" to refer to the multitude of biochemical interactions which can give rise to the piece by piece architectural resetting of filament networks. We believe that our analysis of networks in the presence of this filament recycling will be useful in further developing the qualitative and quantitative understanding the deformation of these complex networks.

Supporting Information

S1 Text. Bold the title sentence. Add descriptive text after the title of the item (optional).

S1 Fig. Bold the title sentence. Add descriptive text after the title of the item (optional).

S2 Fig. Mechanical properties of passive networks. a) Elastic modulus of networks. Our measurements closely match prediction of $G_0 \sim \mu/l_c$. **b)** Placeholder for inevitably another figure relevant to passive properties..

S3 Fig. Mechanical properties of active networks Add descriptive text after the title of the item (optional).

S6 Fig. Spatial velocity profile of networks containing passive and active domains.

S1 Table. Lorem Ipsum. Maecenas convallis mauris sit amet sem ultrices gravida. Etiam eget sapien nibh. Sed ac ipsum eget enim egestas ullamcorper nec euismod ligula. Curabitur fringilla pulvinar lectus consectetur pellentesque.

S1 Video. Extensional strain in passive networks. Movie of simulation setup shown in Figure 2

S2 Video. Active networks contracting with free boundaries. Movie of simulation setup shown in Figure 5

Acknowledgments

We would like to thank Shiladitya Banerjee and Patrick McCall for stimulating discussions.

References

Alvarado et al., 2013. Alvarado, J., Sheinman, M., Sharma, A., MacKintosh, F. C., and Koenderink, G. H. (2013). Molecular motors robustly drive active gels to a critically connected state. *Nat Phys*, 9(9):591–597.

Banerjee and Marchetti, 2011. Banerjee, S. and Marchetti, M. C. (2011). Instabilities and oscillations in isotropic active gels. *Soft Matter*, 7:463–473.

Banerjee et al., 2011. Banerjee, S., Marchetti, M. C., and Müller-Nedebock, K. (2011). Motor-driven dynamics of cytoskeletal filaments in motility assays. *Phys. Rev. E*, 84:011914.

Bausch et al., 1998. Bausch, A. R., Ziemann, F., Boulbitch, A. A., Jacobson, K., and Sackmann, E. (1998). Local measurements of viscoelastic parameters of adherent cell surfaces by magnetic bead microrheometry. *Biophysical Journal*, 75(4):2038 – 2049.

Bois et al., 2011. Bois, J. S., Jülicher, F., and Grill, S. W. (2011). Pattern formation in active fluids. *Phys. Rev. Lett.*, 106:028103.

Bray and White, 1988. Bray, D. and White, J. (1988). Cortical flow in animal cells. *Science*, 239(4842):883–888.

Broedersz et al., 2010. Broedersz, C. P., Depken, M., Yao, N. Y., Pollak, M. R., Weitz, D. A., and MacKintosh, F. C. (2010). Cross-link-governed dynamics of biopolymer networks. *Phys. Rev. Lett.*, 105:238101.

Broedersz et al., 2009. Broedersz, C. P., Storm, C., and MacKintosh, F. C. (2009). Effective-medium approach for stiff polymer networks with flexible cross-links. *Phys. Rev. E*, 79:061914.

Chandran and Mofrad, 2010. Chandran, P. L. and Mofrad, M. R. K. (2010). Averaged implicit hydrodynamic model of semiflexible filaments. *Phys. Rev. E*, 81:031920.

Dierkes et al., 2014. Dierkes, K., Sumi, A., Solon, J., and Salbreux, G. (2014). Spontaneous oscillations of elastic contractile materials with turnover. *Phys. Rev. Lett.*, 113:148102.

Evans and Yeung, 1989. Evans, E. and Yeung, A. (1989). Apparent viscosity and cortical tension of blood granulocytes determined by micropipet aspiration. *Biophysical Journal*, 56(1):151–160.

Filippov et al., 2004. Filippov, A. E., Klafter, J., and Urbakh, M. (2004). Friction through dynamical formation and rupture of molecular bonds. *Phys. Rev. Lett.*, 92:135503.

Head et al., 2003. Head, D. A., Levine, A. J., and MacKintosh, F. C. (2003). Deformation of cross-linked semiflexible polymer networks. *Phys. Rev. Lett.*, 91:108102.

Heisenberg and Bellaïche, 2013. Heisenberg, C.-P. and Bellaïche, Y. (2013). Forces in tissue morphogenesis and patterning. *Cell*, 153(5):948 – 962.

Hiraiwa and Salbreux, 2015. Hiraiwa, T. and Salbreux, G. (2015). Role of turn-over in active stress generation in a filament network. *ArXiv e-prints*.

Hird and White, 1993. Hird, S. N. and White, J. G. (1993). Cortical and cytoplasmic flow polarity in early embryonic cells of caenorhabditis elegans. *The Journal of Cell Biology*, 121(6):1343–1355.

Hochmuth, 2000. Hochmuth, R. M. (2000). Micropipette aspiration of living cells. *Journal of Biomechanics*, 33(1):15 – 22.

Keren et al., 2009. Keren, K., Yam, P. T., Kinkhabwala, A., Mogilner, A., and Theriot, J. A. (2009). Intracellular fluid flow in rapidly moving cells. *Nat Cell Biol*, 11(10):1219–1224.

Kim et al., 2014. Kim, T., Gardel, M. L., and Munro, E. (2014). Determinants of fluidlike behavior and effective viscosity in cross-linked actin networks. *Biophysical Journal*, 106(3):526 – 534.

Kim et al., 2011. Kim, T., Hwang, W., and Kamm, R. D. (2011). Dynamic role of cross-linking proteins in actin rheology. *Biophysical Journal*, 101(7):1597–1603.

Koenderink et al., 2009. Koenderink, G. H., Dogic, Z., Nakamura, F., Bendix, P. M., MacKintosh, F. C., Hartwig, J. H., Stossel, T. P., and Weitz, D. A. (2009). An active biopolymer network controlled by molecular motors. *Proceedings of the National Academy of Sciences of the United States of America*, 106(36):15192–15197.

Köhler and Bausch, 2012. Köhler, S. and Bausch, A. R. (2012). Contraction mechanisms in composite active actin networks. *PLoS ONE*, 7(7):e39869.

Lenz, 2014. Lenz, M. (2014). Geometrical origins of contractility in disordered actomyosin networks. *Phys. Rev. X*, 4:041002.

Lenz et al., 2012. Lenz, M., Gardel, M. L., and Dinner, A. R. (2012). Requirements for contractility in disordered cytoskeletal bundles. *New Journal of Physics*, 14(3):033037.

Lieleg and Bausch, 2007. Lieleg, O. and Bausch, A. R. (2007). Cross-linker unbinding and self-similarity in bundled cytoskeletal networks. *Phys. Rev. Lett.*, 99:158105.

Lieleg et al., 2008. Lieleg, O., Claessens, M. M. A. E., Luan, Y., and Bausch, A. R. (2008). Transient binding and dissipation in cross-linked actin networks. *Phys. Rev. Lett.*, 101:108101.

Lieleg et al., 2009. Lieleg, O., Schmoller, K. M., Claessens, M. M. A. E., and Bausch, A. R. (2009). Cytoskeletal polymer networks: Viscoelastic properties are determined by the microscopic interaction potential of cross-links. *Biophysical Journal*, 96(11):4725–4732.

Liu et al., 2007. Liu, J., Koenderink, G. H., Kasza, K. E., MacKintosh, F. C., and Weitz, D. A. (2007). Visualizing the strain field in semiflexible polymer networks: Strain fluctuations and nonlinear rheology of f-actin gels. *Phys. Rev. Lett.*, 98:198304.

Liverpool et al., 2009. Liverpool, T. B., Marchetti, M. C., Joanny, J.-F., and Prost, J. (2009). Mechanical response of active gels. *EPL (Europhysics Letters)*, 85(1):18007.

Mak et al., 2016. Mak, M., Zaman, M. H., Kamm, R. D., and Kim, T. (2016). Interplay of active processes modulates tension and drives phase transition in self-renewing, motor-driven cytoskeletal networks. *Nat Commun*, 7.

Marchetti et al., 2013. Marchetti, M. C., Joanny, J. F., Ramaswamy, S., Liverpool, T. B., Prost, J., Rao, M., and Simha, R. A. (2013). Hydrodynamics of soft active matter. *Rev. Mod. Phys.*, 85:1143–1189.

Mayer et al., 2010. Mayer, M., Depken, M., Bois, J. S., Julicher, F., and Grill, S. W. (2010). Anisotropies in cortical tension reveal the physical basis of polarizing cortical flows. *Nature*, 467(7315):617–621.

McCrum et al., 1997. McCrum, N., Buckley, C., and Bucknall, C. (1997). *Principles of Polymer Engineering*. Oxford science publications. Oxford University Press.

Müller et al., 2014. Müller, K. W., Bruinsma, R. F., Lieleg, O., Bausch, A. R., Wall, W. A., and Levine, A. J. (2014). Rheology of semiflexible bundle networks with transient linkers. *Phys. Rev. Lett.*, 112:238102.

Munro et al., 2004. Munro, E., Nance, J., and Priess, J. R. (2004). Cortical flows powered by asymmetrical contraction transport {PAR} proteins to establish and maintain anterior-posterior polarity in the early c. elegans embryo. *Developmental Cell*, 7(3):413 – 424.

Murrell and Gardel, 2012. Murrell, M. P. and Gardel, M. L. (2012). F-actin buckling coordinates contractility and severing in a biomimetic actomyosin cortex. *Proceedings of the National Academy of Sciences*, 109(51):20820–20825.

Ndlec et al., 1997. Ndlec, F. J., Surrey, T., Maggs, A. C., and Leibler, S. (1997). Self-organization of microtubules and motors. *Nature*, 389(6648):305–308.

Robin et al., 2014. Robin, F. B., McFadden, W. M., Yao, B., and Munro, E. M. (2014). Single-molecule analysis of cell surface dynamics in caenorhabditis elegans embryos. *Nat Meth*, 11(6):677–682.

Salbreux et al., 2012. Salbreux, G., Charras, G., and Paluch, E. (2012). Actin cortex mechanics and cellular morphogenesis. *Trends in Cell Biology*, 22(10):536 – 545.

Salbreux et al., 2009. Salbreux, G., Prost, J., and Joanny, J. F. (2009). Hydrodynamics of cellular cortical flows and the formation of contractile rings. *Phys. Rev. Lett.*, 103:058102.

Sanchez et al., 2012. Sanchez, T., Chen, D. T. N., DeCamp, S. J., Heymann, M., and Dogic, Z. (2012). Spontaneous motion in hierarchically assembled active matter. *Nature*, 491(7424):431–434.

Spruijt et al., 2010. Spruijt, E., Sprakel, J., Lemmers, M., Stuart, M. A. C., and van der Gucht, J. (2010). Relaxation dynamics at different time scales in electrostatic complexes: Time-salt superposition. *Phys. Rev. Lett.*, 105:208301.

Surrey et al., 2001. Surrey, T., Nédélec, F., Leibler, S., and Karsenti, E. (2001). Physical properties determining self-organization of motors and microtubules. *Science*, 292(5519):1167–1171.

Turlier et al., 2014. Turlier, H., Audoly, B., Prost, J., and Joanny, J.-F. (2014). Furrow constriction in animal cell cytokinesis. *Biophysical Journal*, 106(1):114 – 123.

Unterberger and Holzapfel, 2014. Unterberger, M. J. and Holzapfel, G. A. (2014). Advances in the mechanical modeling of filamentous actin and its cross-linked networks on multiple scales. *Biomechanics and Modeling in Mechanobiology*, 13(6):1155–1174.

Vanossi et al., 2013. Vanossi, A., Manini, N., Urbakh, M., Zapperi, S., and Tosatti, E. (2013). *Colloquium* : Modeling friction: From nanoscale to mesoscale. *Rev. Mod. Phys.*, 85:529–552.

Wachsstock et al., 1994. Wachsstock, D., Schwarz, W., and Pollard, T. (1994). Cross-linker dynamics determine the mechanical properties of actin gels. *Biophysical Journal*, 66(3, Part 1):801 – 809.

Ward et al., 2015. Ward, A., Hilitski, F., Schwenger, W., Welch, D., Lau, A. W. C., Vitelli, V., Mahadevan, L., and Dogic, Z. (2015). Solid friction between soft filaments. *Nat Mater*, advance online publication:–.

Wilhelm and Frey, 2003. Wilhelm, J. and Frey, E. (2003). Elasticity of stiff polymer networks. *Phys. Rev. Lett.*, 91:108103.

Yao et al., 2011. Yao, N. Y., Becker, D. J., Broedersz, C. P., Depken, M., MacKintosh, F. C., Pollak, M. R., and Weitz, D. A. (2011). Nonlinear viscoelasticity of actin transiently cross-linked with mutant alpha-actinin-4. *Journal of Molecular Biology*, 411(5):1062 – 1071.

Zumdieck et al., 2007. Zumdieck, A., Kruse, K., Bringmann, H., Hyman, A. A., and Jülicher, F. (2007). Stress generation and filament turnover during actin ring constriction. *PLoS ONE*, 2(8):e696.